

## ANALYTICAL MODELING AND ATLAS SIMULATION OF $p^+$ - $Hg_{0.78}Cd_{0.22}Te/n$ - $Hg_{0.78}Cd_{0.22}Te/CdZnTe$ HOMOJUNCTION PHOTODETECTOR FOR LWIR FREE SPACE OPTICAL COMMUNICATION SYSTEM

A. D. D. DWIVEDI

Centre for Applied Physics, Central University of Jharkhand, Brambe Ranchi-835 205, INDIA  
[adddwivedi@gmail.com](mailto:adddwivedi@gmail.com), [itbhu.arun@gmail.com](mailto:itbhu.arun@gmail.com)

Revised 13 April 2011, accepted 24 April 2011

### Abstract

In this paper an analytical modeling of  $p^+$ - $Hg_{0.78}Cd_{0.22}Te/n$ - $Hg_{0.78}Cd_{0.22}Te/CdZnTe$  homojunction photodetector for long wavelength free space optical communication has been reported. The results obtained on the basis of analytical model have been compared and contrasted with the simulated results using ATLAS<sup>TM</sup>. The photodetector has been studied in respect of energy band diagram, electric field profile, doping profile, dark current, resistance area-product, quantum efficiency, spectral response, responsivity and detectivity by analytical method using closed form equations and also been simulated by using device simulation software ATLAS<sup>TM</sup> from SILVACO<sup>®</sup> international.

### I. INTRODUCTION

It has been established that long wavelength infrared (LWIR) region is best suited for free space optical communication system[1]. There are two strategic atmospheric transmission windows in the long wavelength infrared region at 9.6  $\mu m$  and 10.6  $\mu m$  which open up the possibility of exploiting infrared atmospheric transparency windows for free space optical communication. The strategic atmospheric attenuation window at 10.6  $\mu m$  is more immune to adverse weather conditions e.g. fog and haze. Therefore an analytical model for a homojunction photodetector  $p^+$ - $Hg_{0.78}Cd_{0.22}Te/n$ - $Hg_{0.78}Cd_{0.22}Te/CdZnTe$  has been developed to explore the potential of the device for the possible free space optical communication applications at 10.6  $\mu m$ . For this purpose a closed form expression for diffusion current in dark and illuminated condition and for quantum efficiency have been derived by solving diffusion equation using appropriate boundary conditions. Results obtained from closed form expressions have been compared and contrasted from those obtained from ATLAS<sup>TM</sup> simulation.

### II THE PROPOSED STRUCTURE

The proposed  $p^+$ - $n$  homojunction photodetector structure and its energy band diagram showing the different mechanisms (diffusion, generation recombination and tunneling (BTB and TAT)) responsible for dark current is shown in Fig.1. It consists of highly doped  $p^+$ - $Hg_{0.78}Cd_{0.22}Te$  over lightly doped  $n$ - $Hg_{0.78}Cd_{0.22}Te$  which is virtually grown on a suitable substrate such as CdZnTe or sapphire using ATHENA tool of

ATLAS<sup>TM</sup>, device simulation software from SILVACO<sup>®</sup> international. The light has been assumed to be incident on the top  $p^+$ - $Hg_{0.78}Cd_{0.22}Te$  side of the photodetector.

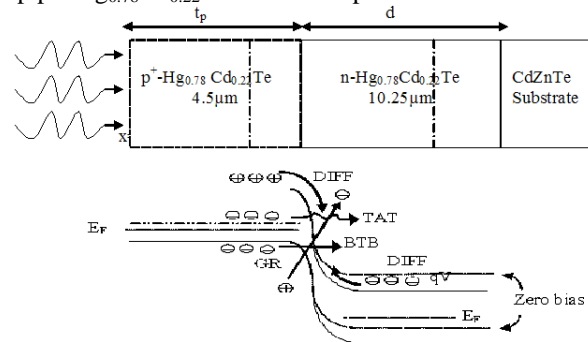


Fig.1 Schematic structure of the proposed  $p^+$ - $Hg_{0.78}Cd_{0.22}Te/n$ - $Hg_{0.78}Cd_{0.22}Te/CdZnTe$  homojunction  $p^+$ - $n$  photodetector and its energy band diagram

The incident light is absorbed in  $p^+$ - $Hg_{0.78}Cd_{0.22}Te$  and  $n$ - $Hg_{0.78}Cd_{0.22}Te$  regions. The operation performance of the  $HgCdTe$  based  $p^+$ - $n$  photodetector has been studied using a two dimensional, drift-diffusion approach utilizing a commercial numerical device simulator ATLAS<sup>TM</sup>. The  $HgCdTe$  based  $p^+$ - $n$  photodiode for long wavelength free space optical communications has been proposed. The numerical simulation of  $p^+$ - $n$  photodetector has been carried out for non degenerate semiconductor and parabolic shape of conduction band. The simulation involves solution of five decoupled equations using Newton's iteration technique. The doping of the regions has been taken analytically uniform for all regions in the above simulation. In calculation of mobility the concentration dependent ANALYTIC model has been considered. For the simulation of dark current, associated with  $p^+$ - $n$  photodetector, AUGER, SRH and OPTICAL (band-to-band) models have been taken into account for recombination mechanisms modeling. Band-to-band standard tunneling model has been considered for tunneling mechanism. The surface recombination process at the contacts has been taken into account in simulation and also in analytical model. The quality of the interface has been characterized in terms of surface recombination velocity. We have taken into account the Fermi-Dirac statistics for parabolic shape of

conduction band in all the calculations of carrier and doping densities.

### III MODELING

#### III.1 Dark Current

The dark current of the p<sup>+</sup>-n photodetector has been modeled here by considering [2] (i) the diffusion of the thermally generated carriers from the neutral regions,  $I_{DIFF}$  (ii) generation-recombination of carriers in the depletion region,  $I_{GR}$  [3] (iii) tunneling of carriers through the barrier,  $I_{TUN}$  [4]. In order to generalize the analysis, we have however considered both trap assisted tunneling (TAT) as well as band-to-band tunneling (BTB). The tunneling component of current thus constitutes two components e.g.,  $I_{TAT}$  arising from the trap assisted tunneling and  $I_{BTB}$  arising out of band-to-band tunneling. The net current can be written as

$$I = I_{DIF} + I_{GR} + I_{TAT} + I_{BTB} \quad (1)$$

#### III.2. Diffusion Current

In the present structure under consideration, the diffusion of minority carriers from both p<sup>+</sup> and n regions, contribute diffusion current. The minority carrier diffusion current under application of a bias voltage,  $V$  can be obtained by solving 1-D diffusion equation under appropriate boundary conditions. Diffusion current density due to holes injected from p<sup>+</sup> region in n-Hg<sub>0.78</sub>Cd<sub>0.22</sub>Te region is modeled as

$$(I_{p/n}) = \frac{qn_i^2 A}{N_D} \sqrt{\frac{\mu_n kT}{q\tau_h}} \frac{\frac{S_p L_p}{D_p} \cosh\left(\frac{d-x_n}{L_n}\right) + \sinh\left(\frac{d-x_n}{L_n}\right)}{\frac{S_p L_p}{D_p} \sinh\left(\frac{d-x_n}{L_n}\right) + \cosh\left(\frac{d-x_n}{L_n}\right)} \left( \exp\left(\frac{qV}{kT}\right) - 1 \right) \quad (2)$$

Diffusion current density due to electrons injected from intrinsic n region in p<sup>+</sup>-Hg<sub>0.78</sub>Cd<sub>0.22</sub>Te region is modeled as

$$(I_{n/p}) = \frac{qn_i^2 A}{N_A} \sqrt{\frac{\mu_n kT}{q\tau_n}} \frac{\frac{S_n L_n}{D_n} \cosh\left(\frac{t-x_p}{L_p}\right) + \sinh\left(\frac{t-x_p}{L_p}\right)}{\frac{S_n L_n}{D_n} \sinh\left(\frac{t-x_p}{L_p}\right) + \cosh\left(\frac{t-x_p}{L_p}\right)} \left( \exp\left(\frac{qV}{kT}\right) - 1 \right) \quad (3)$$

In the above equations,  $n_i$  is the intrinsic carrier concentration of HgCdTe,  $N_A$  and  $N_D$  are the acceptor and donor concentrations in p and n regions respectively,  $q$  is the electronic charge,  $\mu_h$  and  $\mu_n$  are the hole and electron mobility respectively,  $\tau_h$  and  $\tau_n$  are hole and electron life times respectively,  $S_p$  and  $S_n$  are the surface recombination velocities of holes at p-HgCdTe/metal interface and electrons at HgCdTe/CdZnTe hetero-interface and  $L_p$  and  $L_n$  are respective diffusion lengths of holes and electrons on n-

and p-side respectively. Here  $t$  and  $d$  are the thickness of p<sup>+</sup>-HgCdTe and n-HgCdTe regions respectively,  $x_p$  and  $x_n$  are respectively the width of the depletion regions in p and n-regions and  $A$  is the junction area,  $V$  is the applied voltage. The total diffusion current can be written as

$$I_{DIFF} = (I_p)_n + (I_n)_p \quad (4)$$

The product of dynamic resistance and area (RA) is given by the reciprocal of the derivative of the current density with respect to the voltage. The diffusion component of RA product can be obtained as

$$\frac{1}{(RA)_{DIFF}} = \frac{dJ_{DIFF}}{dV} \quad (5)$$

#### III.3 Generation-Recombination Current

The generation-recombination current component arises due to impurities and defects within the depletion region that acts as intermediate states for the thermal generation and recombination of carriers. These intermediate states are known as Shockley-Read-Hall centers. This current could be important than diffusion current, although depletion region is much less than the minority carriers diffusion length, especially at low temperature. The generation-recombination component of current density and associated resistance area product can be approximated as in [3].

#### III.4 Trap-assisted tunneling current

Trap-assisted tunneling occurs when minority carriers tunnel from occupied trap states on quasi neutral side to the empty band states on the other side of the junction or through trap sites present in the depletion region of the junction. These trap centers are intermediate energy levels created by the presence of impurities in the material. The trap-assisted tunneling component of current calculated on the basis of simple one dimensional model and resistance area product associated with trap assisted tunneling can be written as in [5].

#### III.4 Band-to-band tunneling current

When the crossover of energy bands take place at high reverse bias voltage, the band to band tunneling current arises due to flow of electrons from fully occupied valance band of p-region to partially filled or empty states of conduction band of n-region. The band to band tunneling current and band-to-band tunneling component of RA product can be obtained as [2]. Considering the effect of all the two mechanisms discussed above, the net value of the resistance area product can be written as

$$\frac{1}{(RA)_{NET}} = \frac{1}{(RA)_{DIFF}} + \frac{1}{(RA)_{GR}} + \frac{1}{(RA)_{TAT}} + \frac{1}{(RA)_{BTB}} \quad (6)$$

#### III.5 Modeling of carrier lifetime

In order to compute the drift and diffusion components of current accurately, it is necessary to model the lifetime of minority carriers considering all the possible recombination mechanisms. In the present lifetime modeling, we have considered bulk recombination processes in HgCdTe to involve radiative recombination and two non-radiative recombination mechanisms. The direct band-to-band photon assisted recombination is radiative recombination and the phonon assisted recombination processes consists of Auger and Shockley-Read-Hall (SRH) recombination mechanisms which are non-radiative recombination processes. The modeling of the radiative recombination process is straightforward. For direct bandgap HgCdTe semiconductors, the lifetime of carriers due to radiative recombination for low level injection can be approximated as in [6]-[7]. The non-radiative Auger recombination is quite complex. It is an important mechanism in determining the performance of light-emitting devices and infrared detectors made from narrow-gap semiconductors. A semiconductor with a single conduction band and heavy-hole and light-hole valence band there can be at least ten different types of Auger transitions occur. Out of these transitions, the two most significant transitions that occur at the minimum threshold energy ( $E_T \approx E_g$ ) are the Auger-1 or CHCC (involving two conduction band electrons and a heavy hole) and Auger-7 or CHLH (involving one conduction band electron and one heavy hole and one light hole). The former is generally dominant in n-type material and the later in p-type material. The net Auger recombination lifetime of the carriers can thus be written as in [8]. The Auger-1 recombination process involves the direct band-to-band recombination of a conduction band electron with a heavy hole and excitation of another electron in conduction band, dominant in n-type HgCdTe material. The details of computation of the various components of Auger recombination lifetime is discussed in details elsewhere [8].

The lifetime of carriers due to Shockley-Read-Hall recombination can be modeled in terms of trap density and capture cross-section as

$$\tau_{SRH} = \frac{1}{\sigma N_T v_{th}} \quad (7)$$

where  $N_T$  is the SRH trap density,  $\sigma$  is the capture cross-section and  $v_{th}$  is the thermal velocity of the minority carriers in the active region, given by

$$v_{th} = \sqrt{\frac{3kT}{m_n^*}} \quad (8)$$

$m_n^*$  is the effective mass of electrons in the active region. The effective lifetime of the carriers in the active region can be obtained as

$$\frac{1}{\tau_{eff}} = \frac{1}{\tau_{RAD}} + \frac{1}{\tau_{AU}} + \frac{1}{\tau_{SRH}} \quad (9)$$

### III.6 Quantum Efficiency

The quantum efficiency ( $\eta$ ) of a p-n junction photodetector has generally three major components. These components arise from the contribution of the three regions e.g., neutral n-region ( $\eta_n$ ), neutral p-region ( $\eta_p$ ) and the depletion region ( $\eta_{dep}$ ). The optical generation rate of electron-hole pairs, as a function of distance  $x$  from the surface can be written as [9-10]]

$$G(x) = \frac{\alpha(\lambda)(1-R)P_{opt}}{Ah\nu} \exp(-\alpha(\lambda)x) \quad (10)$$

where  $\alpha(\lambda)$  is the optical absorption coefficient of the material which is a function of wavelength  $\lambda$ ,  $R$  is the Fresnel reflection coefficient at the entrance,  $P_{opt}$  is the incident optical power,  $\nu$  is the frequency of radiation and  $A$  is the device area. The quantum efficiency components can be obtained as

$$\eta_n = \frac{(1-R)\alpha L_p}{\alpha^2 L_p^2 - 1} \exp(-\alpha(t_p + x_n)) \left[ \frac{(\gamma_p - \alpha L_p) \exp(-\alpha(d - x_n)) - \left[ \gamma_p \cosh\left(\frac{d - x_n}{L_p}\right) + \sinh\left(\frac{d - x_n}{L_p}\right) \right]}{\gamma_p \sinh\left(\frac{d - x_n}{L_p}\right) + \cosh\left(\frac{d - x_n}{L_p}\right)} + \alpha L_p \right] \quad (11)$$

$$\eta_p = \frac{(1-R) \alpha L_n}{\alpha^2 L_n^2 - 1} \left[ \frac{\alpha L_n + \gamma_n - \exp(-\alpha(t_p - x_p)) \left[ \gamma_n \cosh\left(\frac{t_p - x_p}{L_n}\right) + \sinh\left(\frac{t_p - x_p}{L_n}\right) \right]}{\gamma_n \sinh\left(\frac{t_p - x_p}{L_n}\right) + \cosh\left(\frac{t_p - x_p}{L_n}\right)} - \alpha L_n \exp(-\alpha(t_p - x_p)) \right] \quad (12)$$

where  $L_p$  and  $L_n$  are the hole and electron diffusion lengths in n and p regions respectively.  $\gamma_n = S_n L_n / D_n$  and  $\gamma_p = S_p L_p / D_p$  are the ratio of surface to bulk recombination velocity in p and n regions respectively.

The contribution of the photo-generated carriers in the depletion region to the total quantum efficiency can be obtained as

$$\eta_{dep} = (1-R) \left\{ \exp(-\alpha(t_p - x_p)) - \exp(-\alpha(t_p + x_n)) \right\}$$

The net quantum efficiency can be written as

$$\eta = \eta_n + \eta_p + \eta_{dep} \quad (13)$$

### III.7 Modeling of Specific Detectivity-

The most important figure of merit of the photodetector for use in optical communication is the specific detectivity  $D^*$ , which depends on the wavelength of incident light  $\lambda$ , the quantum efficiency  $\eta$  and zero bias resistance area product,  $R_0 A$ . As the dark current of the detector is contributed by three major components e.g., diffusion, generation-recombination and tunneling (which includes trap assisted tunneling (TAT) and band to band tunneling (BTB)), the detectivity of the photodetector under consideration should be estimated from the net value of  $R_0 A$  product arising out of these mechanism. The specific detectivity of the photodetector which is a function of the applied voltage can be written as [11-12]

$$D^* = \frac{q\eta\lambda}{hc} \sqrt{\frac{(R_0 A)_{NET}}{4kT}} \quad (14)$$

**Responsivity**-The current responsivity ( $\mathcal{R}$ ) of the photodetector is given as [11-12]

$$\mathcal{R} = \frac{q\eta\lambda}{hc} \quad (15)$$

### III.8 Noise Equivalent power-

The variation of noise equivalent power (NEP) with wavelength can be written as

$$NEP = \frac{A^{1/2} B^{1/2}}{D^*} \quad (16)$$

where  $A$  is the area of the detector and  $B$  is the bandwidth, here NEP is calculated at unity bandwidth ( $B=1\text{Hz}$ ).

## IV. RESULTS AND DISCUSSIONS

Numerical computations have been carried out on  $p^+$ - $\text{Hg}_{0.78}\text{Cd}_{0.22}\text{Te}/n$ - $\text{Hg}_{0.78}\text{Cd}_{0.22}\text{Te}/\text{CdZnTe}$  LWIR  $p^+$ n homojunction photodetector at 77K for operation at 10.6  $\mu\text{m}$ . The light has been assumed to be incident on the top  $p^+$ - $\text{Hg}_{0.78}\text{Cd}_{0.22}\text{Te}$  side of the photodetector. The photons with energy higher than the energy gap create electron-hole pairs in p and n region. The mole fraction of cadmium in the ternary MCT material has been calculated so that the bandgap energy of the material corresponds to the long wavelength cut-off value of 10.6  $\mu\text{m}$  for LWIR free space optical communication. The band gap of  $\text{Hg}_{1-x}\text{Cd}_x\text{Te}$  as a function of temperature,  $T$  and alloy composition,  $x$  is included in the simulation model using the empirical formula as in table-1 [13]. The intrinsic carrier concentration was calculated using the expression as in [14]. From Kane band model the hole effective mass is taken as  $m_h^* = 0.55 m_0$  and electron effective mass has been computed following in [15]. The hole mobility has been assumed to be as taken in [13]. The absorption coefficient of  $\text{Hg}_{1-x}\text{Cd}_x\text{Te}$  for optical carrier generation can be calculated within the Kane model, including the Moss-Burstein shift. For photon energy  $E < E_g$  (tail region),  $\alpha < \alpha_g$ , the absorption coefficient obeys the rule [16-17]

$$\alpha = \alpha_0 \exp\left(\frac{\delta(E - E_0)}{kT}\right) \quad (17)$$

And for photon energy  $E > E_g$  (Kane region), the absorption coefficient obeys the rule

$$\alpha = \alpha_g \exp(\beta(E - E_g))^{1/2} \quad (18)$$

where  $\alpha_0$  is the fitting parameter and

$$E_0 = -0.355 + 1.77x \quad (19)$$

$$\frac{\delta}{kT} = \frac{\ln \alpha_g - \ln \alpha_0}{E_g - E_0} \quad (20)$$

$$\alpha_g = -65 + 1.88T + (8694 - 10.315T)x \quad (21)$$

$$\beta = -1 + 0.083 + (21 - 0.13T)x \quad (22)$$

The expressions of the high frequency dielectric constant  $\epsilon_\infty$  and static dielectric constant  $\epsilon_s$  are

obtained as a function of x as in [13].

The parameters used in the computation are listed in Table-1

Parameter	Values
x	0.22
$\Delta$	1 eV
$N_T$	$2.1 \times 10^{19} \text{ m}^{-3}$
$\sigma$	$4.7619 \times 10^{-20} \text{ m}^2$
$N_D$	$1 \times 10^{21} \text{ m}^{-3}$
$N_A$	$1 \times 10^{23} \text{ m}^{-3}$
$M^2$	$10^{-29} \text{ V}^2 \text{ m}^3$
$S_p$	10 m/s
$S_n$	$10^2 \text{ m/s}$
$\chi$	$4.23 - 0.813(E_g - 0.083) \text{ eV}$ [18]
$N_c$	$3.793 \times 10^{22} \text{ m}^{-3}$
$N_v$	$5.1204 \times 10^{24} \text{ m}^{-3}$
$C_n$	$8.3 \times 10^{-32} \text{ m}^6/\text{s}$
$C_p$	$3.33 \times 10^{-31} \text{ m}^6/\text{s}$
$C_C^{OPT}$	$4.87 \times 10^{-16} \text{ m}^6/\text{s}$

The different components of the dark current and RA product have been calculated using the theoretical model discussed in previous section. The variation of quantum efficiency, current responsivity, specific detectivity and Noise equivalent power (NEP) with wavelength at 77 K have been computed from the above mentioned model. The proposed photodetector structure has also been simulated using device simulation software ATLAS<sup>TM</sup> from SILVACO<sup>®</sup> international. The device has been virtually fabricated using ATHENA tool of ATLAS<sup>TM</sup> software from SILVACO<sup>®</sup> international. A program was developed separately for calculation of various characteristics of the photodetector using MATLAB platform by choosing appropriate material parameters.

The simulated results were obtained by developing program in DECKBUILD window interfaced with ATLAS for p<sup>+</sup>-Hg<sub>0.78</sub>Cd<sub>0.22</sub>Te/n<sup>0</sup>-Hg<sub>0.78</sub>Cd<sub>0.22</sub>Te/CdZnTe, homojunction p<sup>+</sup>-n photodetector at 77K. Instead of the graded doping the numerical model includes a uniform doping profile. Once the physical structure of photodetector is built in ATLAS, the properties of the material used in device must be defined. A minimum set of material properties data includes, bandgap, dielectric constant, electron affinity, densities of conduction and valance band states, electron and hole mobility, optical recombination coefficient, and an optical file containing the wavelength dependent refractive index, n [18-21] and extinction coefficient K [18-21] for the used materials. The wavelength dependent values of extinction coefficient K is

computed from the relation, 
$$K = \frac{\alpha \lambda}{4\pi}$$

The energy band diagram has been simulated from BLAZE, which is interfaced with ATLAS is a general purpose 2-D device simulator for III-V, II-VI materials, and devices with position dependent band structure [18]. BLAZE accounts for the effects of positionally dependent band structure by modifications to the charge transport equations. Equilibrium condition energy band diagram for electrons is shown in Fig.2, has been simulated using BLAZE. Equilibrium condition electric field profile of the photodetector is shown in Fig.3. Zero bias doping profile of the device is shown in Fig.4 which shows, position dependent electron and hole concentration inside the device in different regions. Position dependent photogeneration rate at a reverse bias of 0.5V is shown in Fig.5. The optical characteristics of the device have been studied by using LUMINOUS tool of ATLAS device simulator. Primary importance in the simulation of photodetector is the accurate modeling of electron hole pair generation. LUMINOUS, the optoelectronic simulation module in ATLAS, determines the photogeneration at each mesh point in an ATLAS structure by performing two simultaneous calculations. The refractive index  $n$  is used by LUMINOUS to perform an optical ray trace in the device. Difference in  $n$  values across the material boundaries determines the rate of light transmission and reflection. By following the path of light from the source to a mesh point, Luminous is able to determine the optical intensity at that point. Together, these simulations provide for wavelength dependent photogeneration throughout the photodetector [18-19]. The normalized spectral response of the photodetector is shown in Fig.6. It is a plot between normalized terminal current in case of illumination with wavelength of operation. Normalized current increases with wavelength of operation and attains a maximum value at  $\lambda=10.6\mu\text{m}$  and there is a sharp fall beyond  $\lambda=10.6\mu\text{m}$  which is longer cut off wavelength for the proposed composition of the  $\text{Hg}_{1-x}\text{Cd}_x\text{Te}$ , which is absorbing layer in the proposed photodetector. Normalized frequency response of the photodetector is shown in Fig.7. The device exhibits a 3-dB bandwidth more than 10 GHz. All the results discussed above have been obtained by ATLAS simulation. Fig.8 shows variation of dark current with voltage as obtained from analytical model and ATLAS simulation. It is clear from this figure that there is a good agreement between dark current obtained from analytical model and that obtained from ATLAS simulation and device exhibits very low dark current of the order of  $2 \times 10^{-11}$  A.

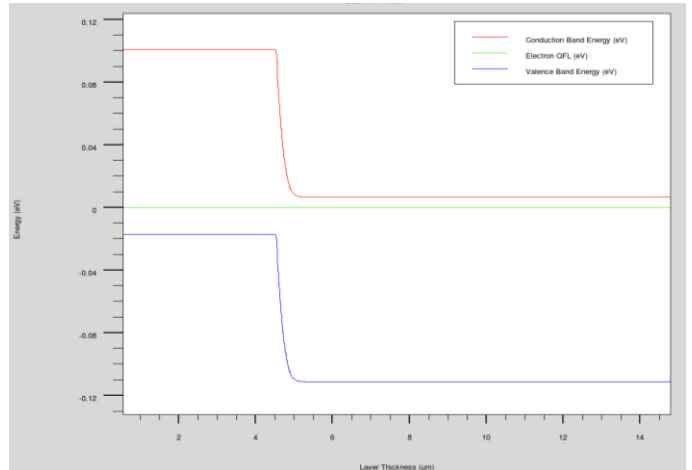


Fig.2 Equilibrium condition energy band diagram of the proposed  $p^+-\text{Hg}_{0.78}\text{Cd}_{0.22}\text{Te}/n^0-\text{Hg}_{0.78}\text{Cd}_{0.22}\text{Te}/\text{CdZnTe}$ , homojunction  $p^+-n$  photodetector

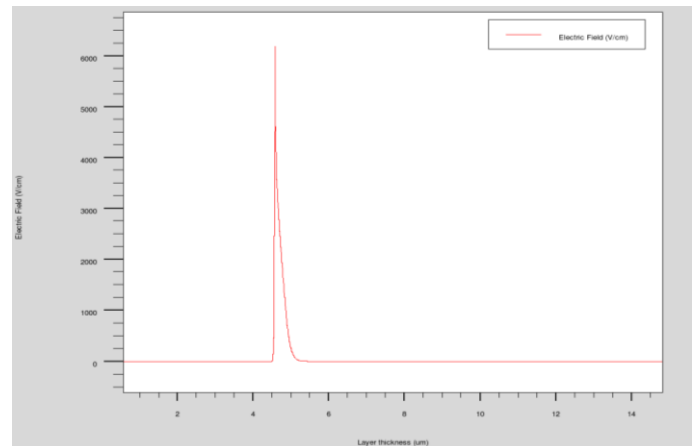


Fig.3 Equilibrium condition electric field profile

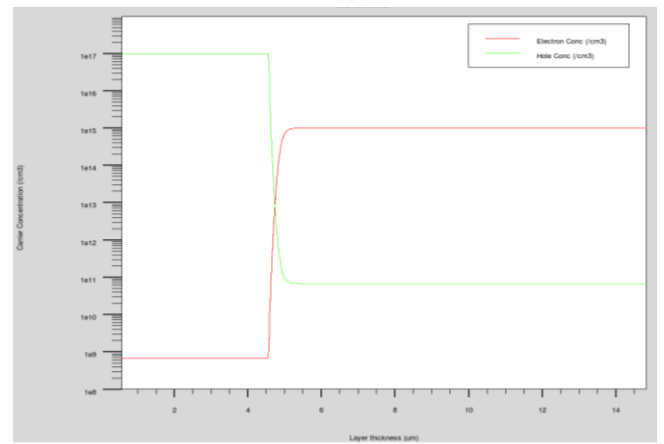


Fig.4 Equilibrium electron and hole concentration profile of the proposed  $p^+-\text{Hg}_{0.78}\text{Cd}_{0.22}\text{Te}/n^0-\text{Hg}_{0.78}\text{Cd}_{0.22}\text{Te}/\text{CdZnTe}$ , homojunction  $p^+-n$  photodetector

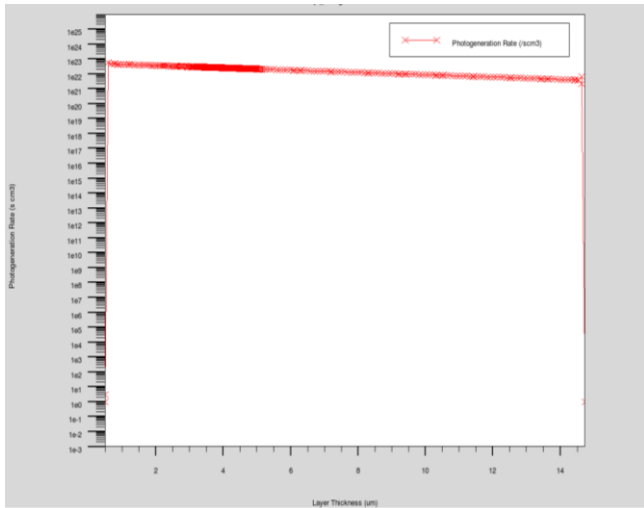


Fig.5 Variation of photogeneration rate with device layer thickness

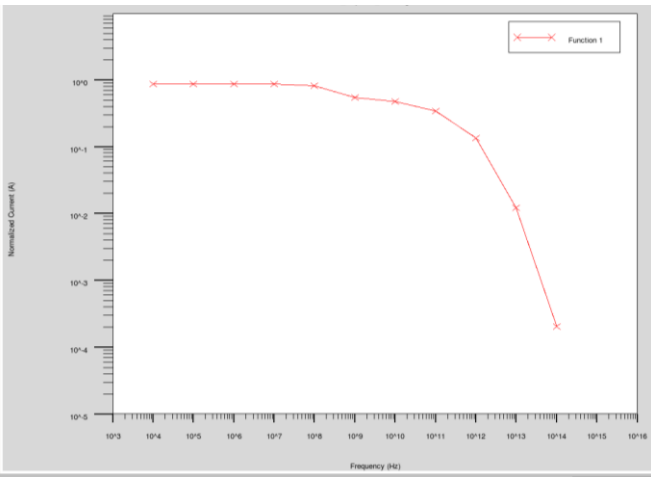


Fig.7 Frequency response of the photodetector

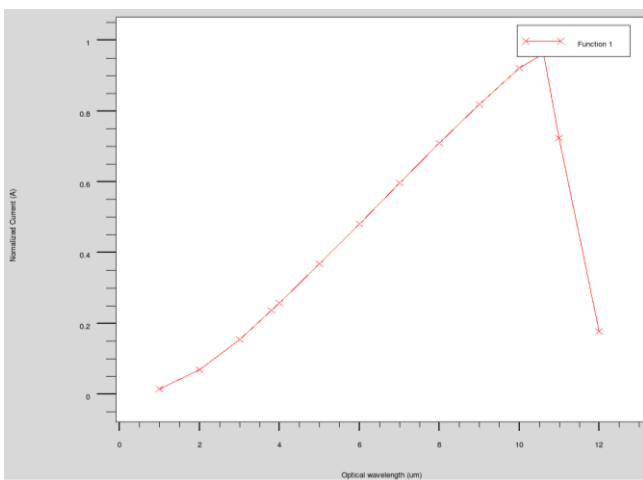


Fig.6 Normalized spectral response of the photodetector

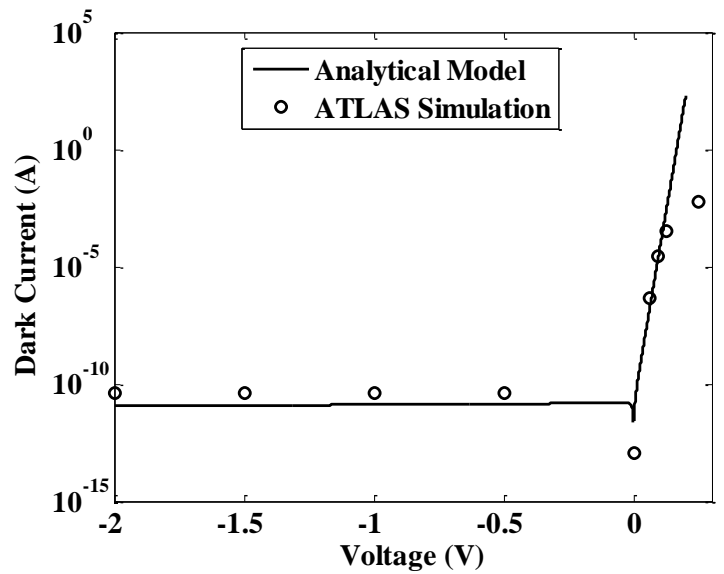


Fig.8 Variation of dark current with bias voltage

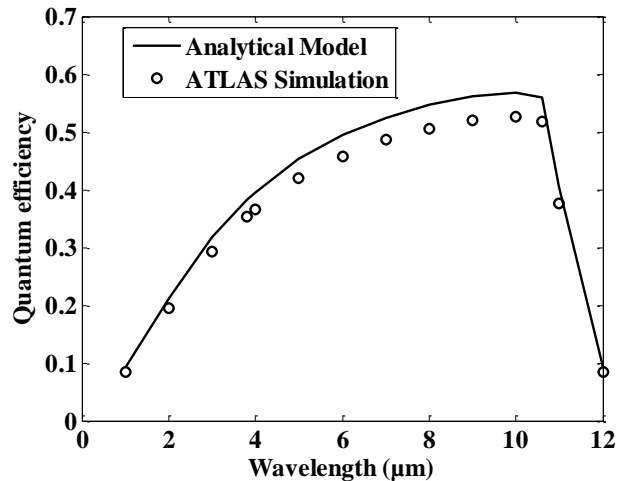


Fig.9 Variation of quantum efficiency with wavelength of operation  
 Variation of quantum efficiency of p-i-n photodetector with wavelength of operation obtained from analytical model and ATLAS simulation at a bias voltage of 0.5V is shown in Fig.9. The device exhibits quantum efficiency of the order of 50% at the desired wavelength of operation 10.6  $\mu\text{m}$  and there is a sharp fall beyond the longer cut-off wavelength 10.6  $\mu\text{m}$  and QE also falls at lower wavelength of operation. From this figure it is clear that there is a good agreement between quantum efficiency obtained by analytical model and that obtained by ATLAS simulation. The device exhibits 50% quantum efficiency at the desired wavelength of operation and at a reverse bias of 0.5V. The variation of responsivity of the photodetector with wavelength of operation is shown in Fig.10. From this figure we can see that there is a very good agreement between responsivity obtained from analytical model and those obtained from ATLAS simulation. The device exhibits very high values of responsivity  $\sim 4.75\text{A/W}$  at wavelength  $10.6\mu\text{m}$  and a bias voltage of 0.5V. Fig. 11 shows variation of specific detectivity with wavelength of operation, obtained by analytical model and also by ATLAS simulation which

indicates that order of detectivity values obtained by analytical model and those obtained by ATLAS simulation are very close.

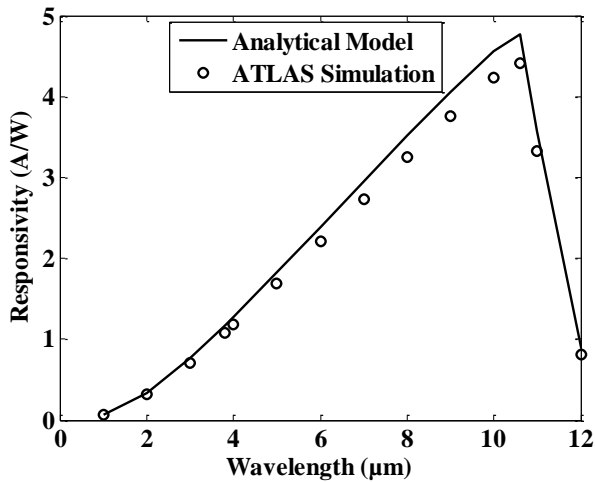


Fig.10 Variation of responsivity with wavelength of operation

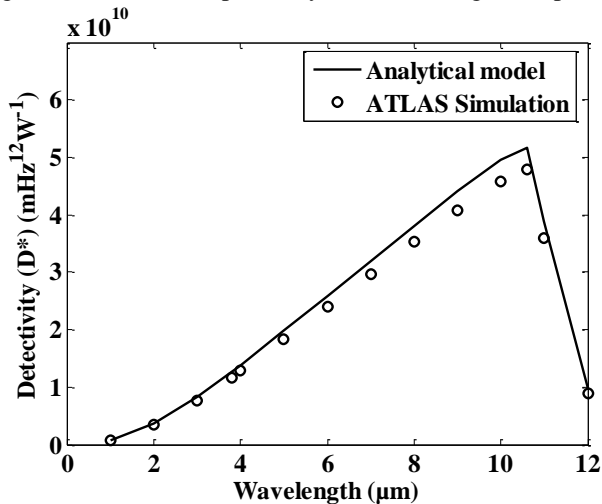


Fig.11 Variation of specific detectivity with wavelength of operation

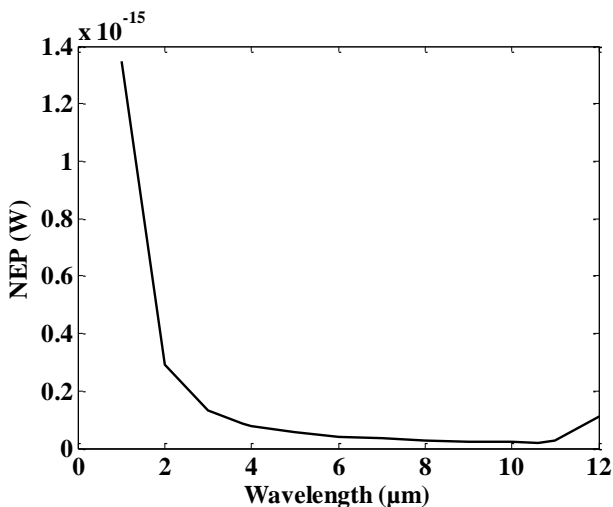


Fig.12 variation of noise equivalent power with wavelength of operation

The device exhibits very high value of specific detectivity  $\sim 5 \times 10^{10} \text{ mHz}^{1/2} \text{W}^{-1}$  at the desired wavelength of operation  $10.6 \mu\text{m}$  and a bias voltage of  $0.5 \text{V}$ .

Fig.12 shows variation of noise equivalent power of the photodetector with wavelength of operation. We can see that the device exhibits a very low value of noise equivalent power (NEP) of the order of  $\sim 10^{-16} \text{ W}$  at the desired wavelength of operation  $10.6 \mu\text{m}$  and NEP increases drastically at smaller wavelengths ( $< 2 \mu\text{m}$ ) and it also increases beyond the upper cut off wavelength  $10.6 \mu\text{m}$  of the detector.

## V. CONCLUSION

The performance of the device has been examined by developing an analytical model for the dark current, quantum efficiency, responsivity and detectivity and results obtained from analytical model have been compared and contrasted by those obtained from ATLAS™ device simulation software from SILVACO® international. There is a very good agreement between results obtained by analytical model and those obtained from ATLAS simulation. The device exhibited a very low dark current of the order of  $2 \times 10^{-11} \text{ A}$ , quantum efficiency  $\sim 50\%$ , responsivity  $\sim 4.75 \text{ A/W}$ , detectivity  $\sim 5 \times 10^{10} \text{ mHz}^{1/2} \text{W}^{-1}$  and noise equivalent power (NEP)  $\sim 10^{-16} \text{ W}$  at wavelength of operation  $10.6 \mu\text{m}$  and bias voltage of  $0.5 \text{V}$ .

## References

1. Haim Manor and Shlomi Arnon, "Performance of an optical wireless communication system as a function of wavelength," *Applied Optics*, vol. 42 No. 21, 2003.
2. J.V.Gumenjuk-Sichevskaya and F.F.Sizov, "Currents in narrow-gap photodiodes," *Semicond. Sci. Technol*, vol. 14, pp.1124-1131, 1999.
3. R. Schoolar, S. Price, and J. Rosbeck, "Investigation of the generation-recombination currents in HgCdTe mid wavelength infrared photodiodes," *J. Vac. Sci. Technol. B*, vol. 10, pp. 1507-1514, 1992.
4. A.Unikovski and Y.Nemirovski "Trap-assisted tunneling in HgCdTe photodiode," *Appl.Phys.Lett.*, vol. 61 (3), pp. 330-332, 1992.
5. V. Gopal, S. K. Singh and R.M. Mehra, "Analysis of dark current contributions in mercury cadmium telluride junction diodes," *Infrared Physics and Technology*, Vol.43, pp.317-326, 2002.
6. V.C.Lopes, A.J.Syllaios and M.C.Chen, "Minority carrier lifetime in mercury cadmium telluride," *Semicond. Sci. Technol.*, vol. 8, pp 824-841, 1993.
7. S.H.Shin, J.M.Arias, M. Zandian, J.G.Pasko and R.E.DeWames, "Effect of the dislocation density on

- minority-carrier lifetime in molecular beam epitaxial HgCdTe,” *Appl. Phys. Lett.*, vol. 59 (21), 18 November 1991.
8. S. Krishnamurthy and T.N. Casselman, “A Detailed Calculation of the Auger Lifetime in p-Type HgCdTe,” *Journal of Electronic Materials*, vol. 29 (6), pp. 828-831, 2000.
  9. Y. Tian, B. Zhang, T. Zhan, H. Jiang, and Y. Jin, “Theoretical analysis of the detectivity in N-p and P-n GaSb/GaInAsSb infrared photo-detectors,” *IEEE Trans. Electron Dev.*, vol. ED-47, pp. 544-551, 2000.
  10. P. Chakrabarti, A. Krier, and A. F. Morgan, “Analysis and simulation of a mid-infrared P<sup>+</sup>-InAs<sub>0.55</sub>Sb<sub>0.15</sub>P<sub>0.30</sub>/n<sup>0</sup>-InAs<sub>0.89</sub>Sb<sub>0.11</sub>/N<sup>+</sup>-InAs<sub>0.55</sub>Sb<sub>0.15</sub>P<sub>0.30</sub> double heterojunction photodetector grown by LPE,” *IEEE Trans. Electron Devices*, vol. ED-50, pp. 2049-2058, 2003.
  11. A.D.D. Dwivedi, Arun Kumar Singh, Rajiv Prakash and P. Chakrabarti, “A Proposed Organic Schottky Barrier Photodetector for application in the Visible Region,” *Current Applied Physics*, Vol. 10, pp. 900-903, 2010.
  12. Arun Kumar Singh, A. D. D. Dwivedi, P. Chakrabarti and Rajiv Prakash, “Electronic and Optical Properties of Electrochemically Polymerized Polycarbazole/Aluminum Schottky Diodes,” *Journal of Applied Physics*, Vol.105, 114506 (2009).
  13. A. Rogalski, K. Adamiec and J. Rutokowski, “Narrow-gap semiconductor photodiodes,” SPIE Press, Bellingham, Washington, USA, 2000.
  14. P. Capper, Properties of Narrow Gap Cadmium-Based Compounds, EMIS data reviews series, No. 10, INSPEC, The institution of Electrical Engineers, London, 1995.
  15. M.H. Weiler, “Magneto-optical properties of Hg<sub>1-x</sub>Cd<sub>x</sub>Te Alloyed,” in *Semiconductors and Semimetals*, edited by R.K. Willardson And A.C. Beer, Academic Press, New York Vol.16, pp 119-191, (1981).
  16. J. Chu, Z. Mi, and D. Tang, “Band-to band absorption in narrow-gap Hg<sub>1-x</sub>Cd<sub>x</sub>Te semiconductors,” *J. Appl. Phys.* Vol. 71, pp.3955-3961 (1992).
  17. J. Chu, B. li, K. Liu and D. Tang, “Empirical rule of intrinsic absorption spectroscopy in Hg<sub>1-x</sub>Cd<sub>x</sub>Te,” *J. Appl. Phys.* Vol.75, pp.1234-1235 (1994).
  18. ATLAS User’s manual Version 5.10.0.R, SILVACO International, Santa Clara, CA 95054, 2005.
  19. A. D. D. Dwivedi and P. Chakrabarti, “Modeling and ATLAS simulation of HgCdTe based MWIR photodetector for free space optical communication,” *International Conference on Recent Advances in Microwave Theory and Applications (MICROWAVE-2008)*, pp.412 – 415, 21-24, November 2008.
  20. A.D.D. Dwivedi, A. Mittal, A. Agrawal and P. Chakrabarti, “Analytical Modeling and ATLAS Simulation of N<sup>+</sup>-InP/n<sup>0</sup>-In<sub>0.53</sub>Ga<sub>0.47</sub>As/p<sup>+</sup>In<sub>0.53</sub>Ga<sub>0.47</sub>As p-i-n Photodetector for Optical Fiber Communication,” *Infrared Physics & Technology*, Vol. 53, no. 4, p. 236-245 (2010).
  21. A.D.D. Dwivedi and P. Chakrabarti, “Analytical Modeling and ATLAS Simulation of N<sup>+</sup>-Hg<sub>0.69</sub>Cd<sub>0.31</sub>Te /n<sup>0</sup>-Hg<sub>0.78</sub>Cd<sub>0.22</sub>Te/p<sup>+</sup>Hg<sub>0.78</sub>Cd<sub>0.22</sub>Te p-i-n Photodetector for Long wavelength Free Space Optical Communication,” *Optoelectronics and Advanced Materials-Rapid Communications (OAM-RC)*, Vol. 4, no-4, pp. 480-497, (2010).